NUMERICAL SIMULATIONS FOR PREPARING NEW AERO-STRUCTURAL DYNAMIC EXPERIMENTS IN ETW WITH A MODIFIED HIRENASD WING MODEL

B.-H. Chen[1], K.-H. Brakhage[2], M. Behr[3], and J. Ballmann[4]

[1]LFM/CATS, RWTH Aachen University
Schinkelstr. 2, 52062 Aachen, Germany
chen@cats.rwth-aachen.de

[2]IGPM, RWTH Aachen University
Templergraben 55, 52062 Aachen, Germany
brakhage@igpm.rwth-aachen.de

[3]CATS, RWTH Aachen University
Schinkelstr. 2, 52062 Aachen, Germany
behr@cats.rwth-aachen.de

[4]LFM, RWTH Aachen University
Schinkelstr. 2, 52062 Aachen, Germany
ballmann@lufmech.rwth-aachen.de

Keywords. IFASD, Steady/Unsteady Aeroelasticity, Aero Structural Dynamics, Methods for Airplane Design

Abstract. In this paper preliminary numerical investigations are presented which have been conducted at the Chair of Mechanics (LFM[3]) of RWTH Aachen University during the course of the new experimental/numerical project Aero-Structural Dynamics Methods for Airplane Design (ASDMAD). The goal was to study the static and dynamic behaviour of the modified HIRENASD wing. After a short introduction of the project specifications the numerical method and model are described. The calculated results are compared with those of the original HIRENASD model, and conclusions are drawn with respect to the differences between the two models.

1 INTRODUCTION

The following up project ASDMAD (Aero-Structural Dynamics Methods for Airplane Design) of the High Reynolds Number Aero-Structural Dynamics (HIRENASD) project is aimed at the further development of new computational and experimental methods of Aero-Structural Dynamics (ASD) to tools for the design of large passenger aircrafts. The CASD package SOFIA developed at RWTH Aachen University within the frame of the Collaborative Research Centre "Flow Modulation and Fluid-Structure Interaction at Airplane Wings" (SFB 401) forms the basis for the computational tool and the preparation of new experiments in the European Transonic Wind Tunnel (ETW) under cryogenic conditions to achieve high Reynolds numbers. In the more recent past SOFIA has been used for the design and analysis of a wind tunnel wing model and validated successfully against *static* and *dynamic* aeroelastic experiments in *subsonic* flow, conducted within the SFB 401's central HIRENASD project [1–6].

---

[3]has meanwhile merged into Chair for Computational Analysis of Technical Systems (CATS)

For the new experiments in ASDMAD the SFB 401 will provide its elastic wing model, which has a 34° leading edge sweep and was developed, built and equipped with measuring techniques within the frame of the HIRENASD project, and tested in ETW. Figure 1 shows the planned test envelope in ASDMAD for Ma=0.80. In the new test campaign the experimental investigations will now concentrate on variations of the Mach number Ma=0.80, 0.83, 0.85, 0.92 and loads factor which is dynamic pressure q over Young's modulus E, q/E=$0.22 \cdot 10^{-6}$, $0.34 \cdot 10^{-6}$, $0.48 \cdot 10^{-6}$ and $0.60 \cdot 10^{-6}$. Furthermore, the Reynolds number now is chosen constant at Re=$23.5 \cdot 10^6$. At this value of the Reynolds number transition is concentrated on the leading edge region such that the flow is fully turbulent over the whole wing surface. The wing model has been redesigned in the tip range to be shortend first and thereafter equipped with different tip devices of which one will be a winglet with aerodynamic control surface (WACS) which can be actuated (ACS). The redesigned wing model will have the same span as the original one.
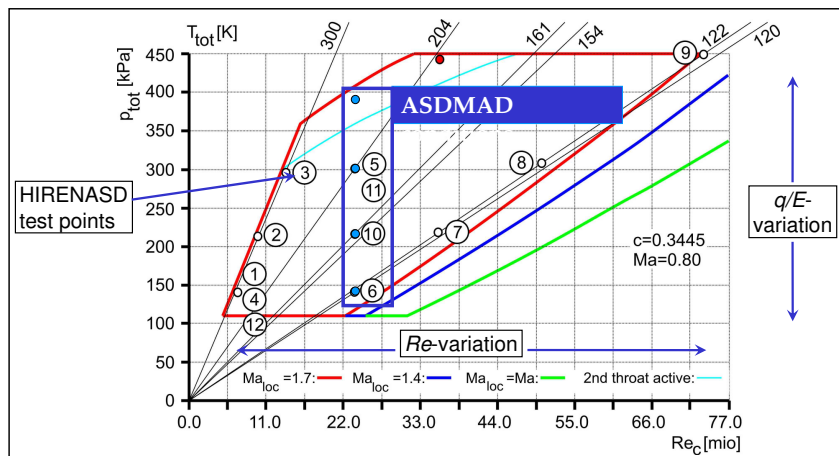

Figure 1: ASDMAD envelope for new test series with winglet configuration at Ma=0.80

The model preparations for the experiments in ETW are currently in progress. In the run-up to the experiments lots of preliminary investigations have been performed, including static and dynamic aeroelastic simulations. The first task within ASDMAD comprised of finding a suitable winglet shape for the wind tunnel model. Therefore, four winglet shapes differing only in the winglet additional sweep angle (0°, 5°, 10°, 15°) have been designed and investigated on aerodynamic performance considering static aeroelastic simulations. The one with about 10 degrees additional sweep was selected in a compromise decision between aerodynamic properties and required internal space for the ACS driving mechanism. For the thus modified wing model extensive static aeroelastic simulations were carried out with and without deflected WACS at angles between -5° and $+5^o$. Aeroelastic equilibrium configurations were investigated to determine the effects resulting from changes of the parameters Mach number Ma, dynamic loads factor q/E, and angle of attack α on aerodynamic design loads. Furthermore, the influence of the WACS on structural loads and flow behaviour was analysed. The pre-examinations further comprised the determination of the vibrational decay behaviour of the wing in dependence on the incident flow. The dynamic response simulations are also carried out with fixed WACS deflection. The results are analysed w.r.t. the aerodynamic influence of the winglet shape and the efficiency of the WACS with regard to its influence on the dynamic wing in comparison to the original HIRENASD model.

2

2 CAE PACKAGE SOFIA

The aeroelastic software package SOFIA follows a partitioned approach, in which separate programs are operated iteratively for the solution of structural deformation and the flow solution on a deforming grid. The Aeroelastic Coupling Module (ACM) [1] which allows for distinct Euler- or Navier-Stokes flow solvers with distinct FE-based structural solvers forms the core of SOFIA. On the one hand it coordinates the sequence of solver calls, and on the other hand the transfer of aerodynamic loads and structural deformations in the mutual directions between flow field and structural partition. For unsteady aeroelastic problems different loose coupling schemes with prediction-/correction steps are available, enhanced by extrapolation techniques for flow and structural deformation states as well as an imperative tight coupling scheme. For steady aeroelastic problems an under-relaxed Gauss-Seidel scheme is used.

The representation of the wing model structure is realised using Timoshenko beam elements which is one of the FE (*Finite Element*) types provided in the in-house FEAFA code (*Finite Element Analysis for Aeroelasticity*). Although, FEAFA offers a full range of FE types comparable to commercial CSM (*Computational Structural Mechanics*) packages, generalised Timoshenko beam elements are preferred for slender aircraft structures due to low computational costs.

All results presented in this paper were obtained using the FLOWer code, developed under the leadership of the German Aerospace Center (DLR) during projects MEGAFLOW I/II [7] and MEGADESIGN [8]. It solves the 3D time-dependent Reynolds Averaged Navier-Stokes (RANS) equations for perfect gases on structured deformable multi-block grids. SOFIA also provides QUADFLOW [9] and TAU [7] as flow solvers. The Linearised Explicit Algebraic (LEA) model, based on the solution of two additional equations, one for the turbulent kinetic energy k and one for the specific dissipation rate ω was used in all CAE simulations to model the turbulence.

For the deformation of multiblock-structured grids (e.g. FLOWer grids) the in-house MUGRIDO code (*Multiblock Grid Deformation Tool*) [10, 11] is applied. It generates a fictitious framework of beams by modelling the CFD block boundaries and a given percentage of grid lines as massless linear elastic Timoshenko beams. These are considered rigidly fixed together in points of intersection and to the aerodynamic surface as well, such that cell angles are preserved where beams, i.e. grid lines, intersect or emerge from a solid surface. The right hand side for the resulting FE problem in MUGRIDO is supplied by the deflections of the wetted surface relative to the undeformed grid. A well shaped volume CFD grid is finally reconstructed from the deformed beam framework by two- and three-dimensional Transfinite Interpolation.

3 WING-WINGLET MODEL REPRESENTATION

3.1 Wind Tunnel Model Specifications

The main part of the new wing model is the shortened HIRENASD model [6], and the half span of almost $1.30m$ is preserved by the new model. The proposed cut-off positions at the HIRENASD model for attaching the winglet are dislocated in order to stiffen the mounting of the winglet parts. An illustration is given in Figure 2.
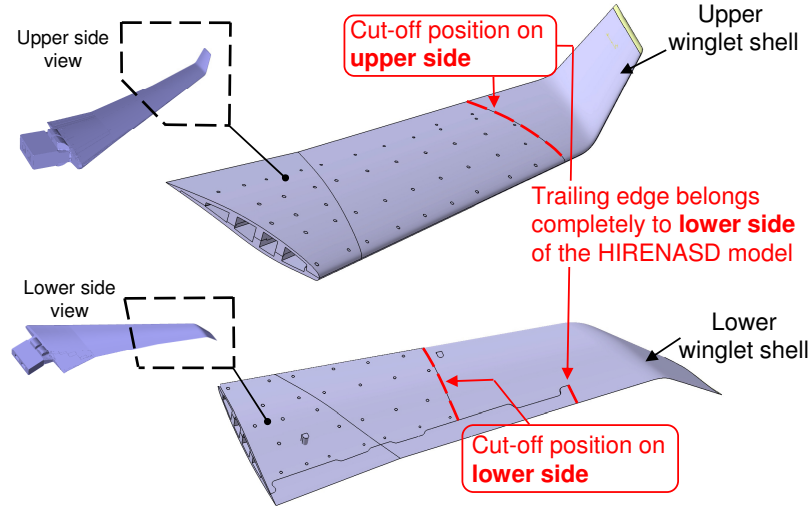
Figure 2: Proposed cut-off positions at the HIRENASD wing

The winglet has a dihedral of 40° and a length of approximately $0.12m$. The geometric properties of the winglet are desribed in detail in Figure 3. Due to space and load limitations, the control surface is limited to a width of $35mm$ and a length of $90mm$. Furthermore, a winglet sweep angle is introduced as an additional parameter.
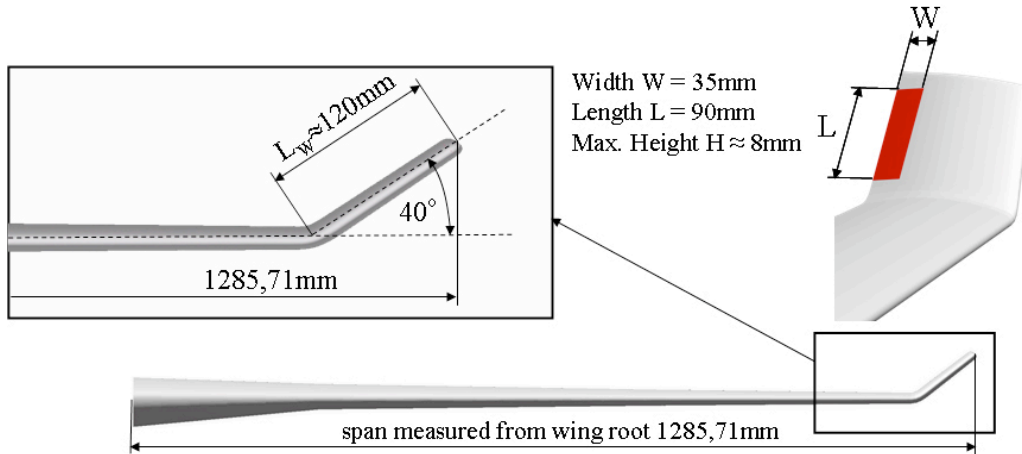

Figure 3: Geomtric properties of the winglet

Figure 4 shows the computational model and the aerodynamic shape of all winglets investigated (presented in section 4.1) in the run-up to the preliminary numerical investigations. The one with the 10° sweep angle additional to the 34° leading edge sweep in the middle right of Figure 4 was selected for the redesign of the wind tunnel model. The additional winglet will also be manufactured from *C200 Maraging Steel* which is the same material as for the HIRENASD model.

3.2 Structural Model

The properties of the wing-winglet structure was idealised using an efficient beam model based on multi-axial Timoshenko beam elements. The structural representation has been
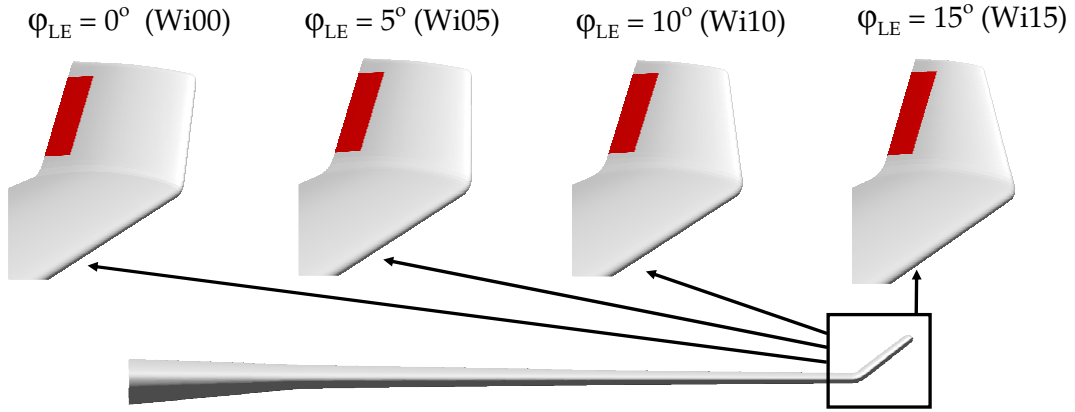
Figure 4: Investigated winglet shapes with different sweep angles

generated by extending the already existing beam identification of the original HIRE-NASD wing model [1,3] by a very stiff winglet part. The aerodynamic surface and beam model of the HIRENASD and ASDMAD wing model are depicted in Figure 5. The beam model is generally divided into two parts, whereas the first part represents the balance and the clamping region including the excitation mechanism and the second part the wing, respectively. The vacuum frequencies of the 1st, 2nd flap-bending and 1st torsion dominated modes of the HIRENASD wing and the redesigned wing are listed in Table 1. Due to the additional stiffness of the winglet part the eigenfrequencies of the flap-bending dominated modes are higher by more than 4%, while the frequency of the 1st torsion dominated mode is lower.
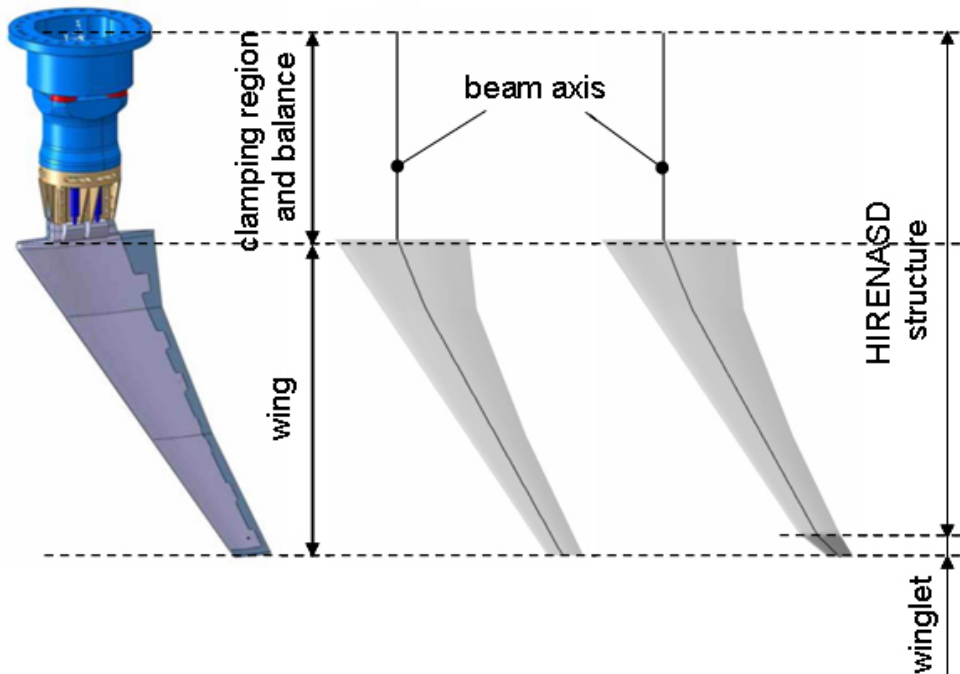

Figure 5: Aerodynamic surface and beam model with additional consideration of balance inertia and elasticity

Mode	Description	$f_{HIRENASD}$ Hz	f_{ASDMAD} Hz	Difference %
1	First bending	26.825	28.072	4.44
2	Second bending	86.752	90.778	4.43
3	First torsion	270.076	262.188	-2.92

Table 1: Vacuum frequencies of HIRENASD and ASDMAD wings at material temperature 173K

3.3 CFD Grid for Flow Simulation

For the numerical investigations a new CFD grid was designed. It constitutes a half-model, whereby only cases with flow conditions symmetrical to the fuselage mid-plane were considered.

The grid depicted in Figure 6 was generated using the program ICEM CFD from ANSYS. It has approximately 1.6 million grid points and 1.4 million cell volumes. The wetted surface has a no-slip condition applied on it. A symmetry plane normal to the wing mid-plane is assumed at the wing root corresponding to an inviscid plane wall. Farfield conditions are fulfilled at the domain boundaries far away from the model. Therefore no influences from wind tunnel walls are considered in this study.
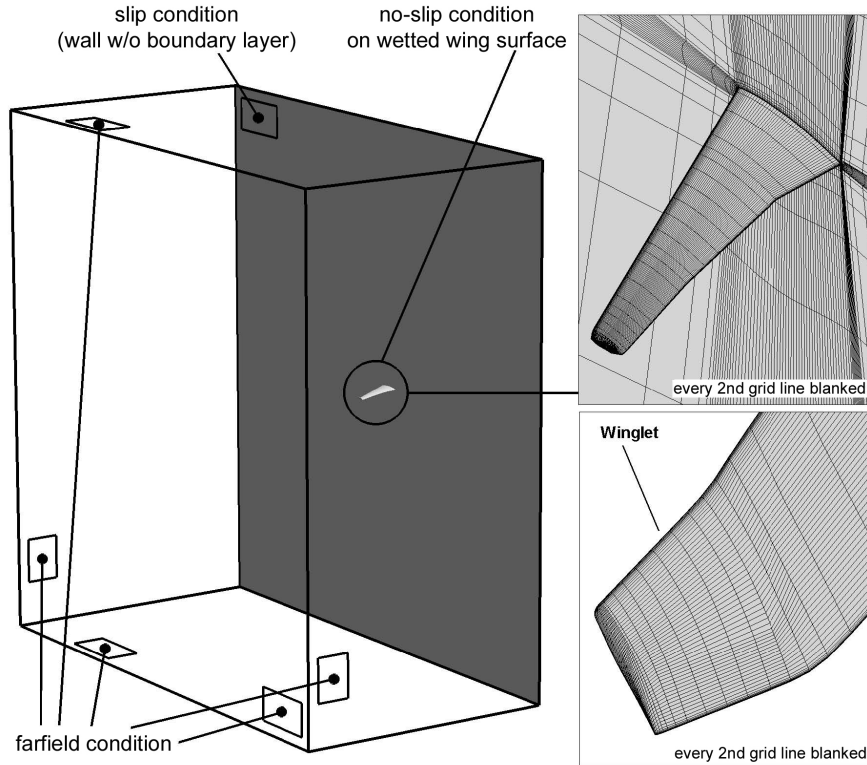

Figure 6: Grid topology, point distribution on wetted model surface and imposed boundary conditions for the flow grid with wing-winglet configuration

4 PREDICTION OF STATIC AEROELASTIC MODEL BEHAVIOUR

4.1 Winglet Sweep Influence on Aerodynamic Performance

As already mentioned four winglet shapes with an additional sweep angle of 0°, 5°, 10° and 15° to the 34° sweep angle of the leading edge have been investigated regarding
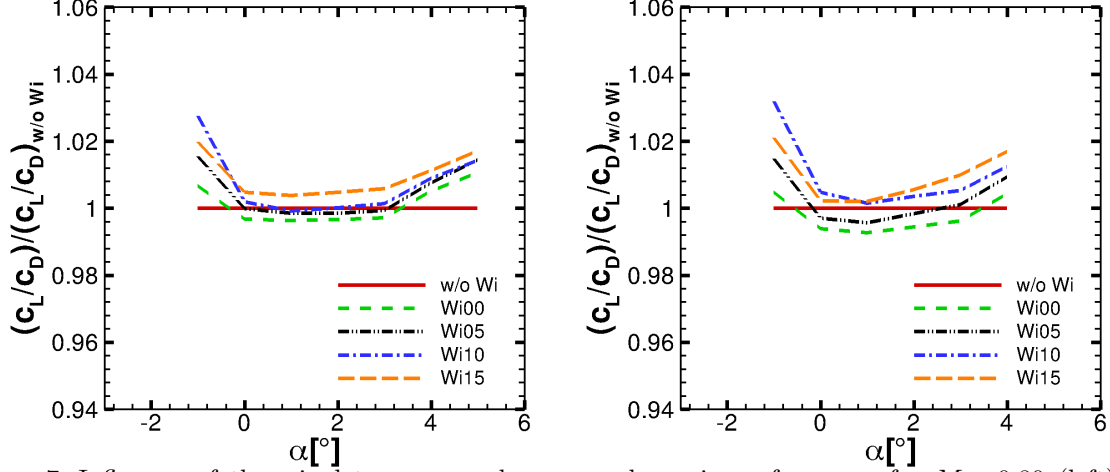
Figure 7: Influence of the winglet sweep angle on aerodynamic performance for Ma=0.80 (left) and Ma=0.83 (right), q/E=0.34 $\cdot$ 10^{-6} and Re=23.5 $\cdot$ 10^{6}

aerodynamic performance by means of aeroelastic equilibrium computations. The angle of attack was varied from α=-2° to $+5^{o}$ in increments of 1° for conditions of the planned test campaign. Figure 7 exhibits the lift to drag ratio of the redesigned wing normalised by the lift to drag ratio of the HIRENASD wing over the angle of attack exemplarily for Ma=0.80 (left) and Ma=0.83 (right), q/E=0.34 $\cdot$ 10^{-6} and Re=23.5 $\cdot$ 10^{6}. Both plots emphasize an increasing lift to drag ratio, thus efficiency of a higher winglet sweep angle for most angles of attack which is even more pronounced for a 10° and 15° swept winglet at Ma=0.83. The winglet with a 10° added sweep shows a positiv lift to drag ratio at both Mach numbers and the overall second best result, behind a 15° sweep which, however, has an insufficient space for the actuator mechanism. Henceforth the winglet variations are labeled "Wi00", "Wi05", "Wi10" and "Wi15" according to their additional sweep angle.

To study the winglet sweep effect resulting from changes of the parameters Ma and q/E in detail only simulations of the wing-winglet configurations "Wi00" and "Wi10" were investigated and compared to the wing configuration without winglet.
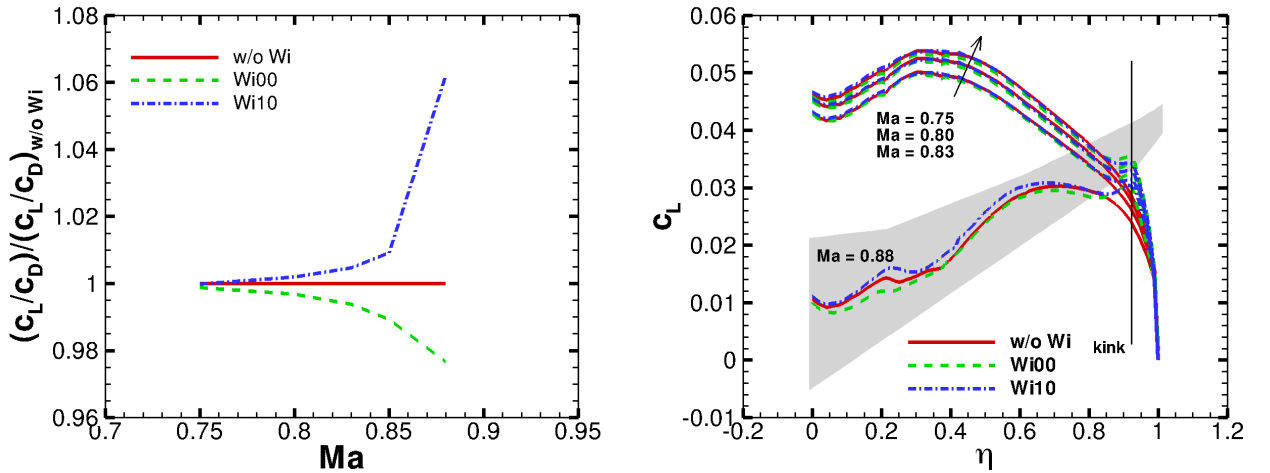

Figure 8: Winglet sweep influence for Mach number and q/E=0.34 $\cdot$ 10^{6}, Re=23.5 $\cdot$ 10^{6}, α=0°, left: lift to drag ratio normalized by lift to drag ratio of wing without winglet, right: spanwise lift distribution

7

The influence of the Mach number variation on the normalised lift to drag ratio is depicted on the left in Figure 8. On the right side of Figure 8 the corresponding spanwise lift distributions are shown. Differences between these three configurations can be observed more clearly at higher Mach numbers and in the winglet area, as the geometric properties of the winglets lead to lift increase with the drawback of higher root bending moments. At Ma=0.88 the advantage of the "Wi10" configurations becomes even more pronounced in both diagrams of Figure 8. On the one hand the lift to drag ratio on the left strongly increases, whereas on the other hand the lift now increases over the whole wing span. Both results emphasize the improved aerodynamic behaviour of the "Wi10" compared to the wing-winglet configuration without additional sweep, particulary at high Mach numbers where the lift to drag ratio normally drops drastically.

4.2 Winglet Sweep Influence on Aeroelastic Equilibrium

In the following results of the winglet sweep influence on the wing deformation characterised by the vertical displacment u_y and aerodynamic twist ϕ_{twist} are discussed. Furthermore, changes in lift polars of the "Wi10" configuration are presented for different angles of attack and variations of Ma and q/E with respect to aeroelasticity.

Figure 9 shows exemplarily a comparison of spanwise wing deformations between computations of the HIRENASD, "Wi00" and "Wi10" configuration. On the left of Figure 9 the vertical displacement is depicted, whereas the results for $\alpha=-2^o$ can be viewed in more detail in the enlargement. The aerodynamic twist for the corresponding flow conditions is shown on the right. Both results exhibit a higher deformation of the configurations with additional winglet compared to the wing without.
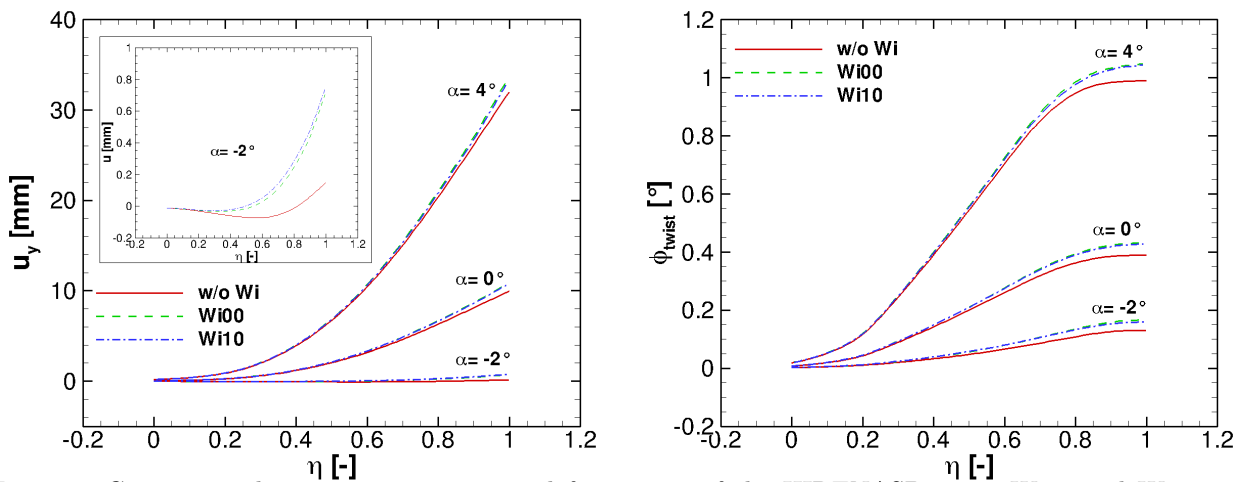

Figure 9: Comparison between spanwise wing deformations of the HIRENASD wing, Wi00 and Wi10 configuration for different angles of attack, left: vertical displacment u_y, right: aerodynamic twist ϕ_{twist} (Ma=0.80, q/E=0.34 $\cdot$ 10^{-6}, Re=23.5 $\cdot$ 10^6)

The planned aeroelastic experiments in ETW comprise independent variations of Ma and q/E. In Figure 10 the impact on the lift polars of the modified wing with 10° additional sweep are plotted. On the left the pure Mach number (Ma=0.80, 0.83, 0.85 and 0.88) influence at constant Re and q/E is illustrated. The diagram on the right of Figure 10 exhibits the lift polars regarding changes of the loads factor q/E. The gradient of c_l-α drops with increasing q/E.
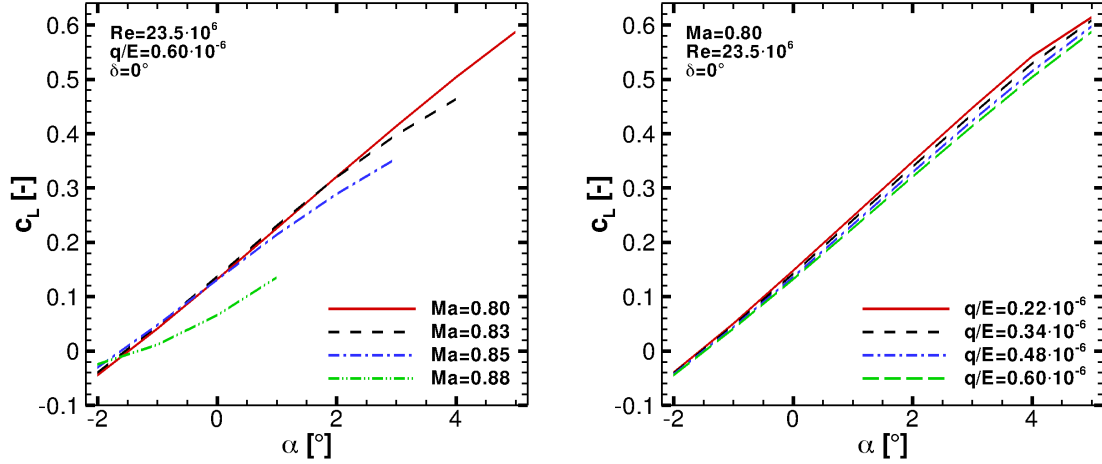
Figure 10: Influence of the Ma and q/E variation on the lift of the Wi10 configuration, left: lift polars due to Ma variation, right: lift polars due to q/E variation for Ma=0.80

4.3 Influence of the Static Control Surface Deflection

The impact of a static control surface deflection at $\delta=-5^o$, $\delta=0^o$ and $\delta=5^o$ on the winglet pressure distrubution is depicted in Figure 11 for the following flow conditions, whereas only results of the "Wi10" configuration are investigated in the following: Ma=0.83, q/E=$0.60 \cdot 10^{-6}$, Re=$23.5 \cdot 10^6$ and α=0°. A positive deflection is defined as inboard deflection, which leads to a decrease of the winglet load as shown in the pressure distribution, thus a reduction of the wing root bending moment. On the contrary a negative deflection increases the winglet load. Therefore the control device appears to be an adequate method to lower the wing root load due to the additional winglet.
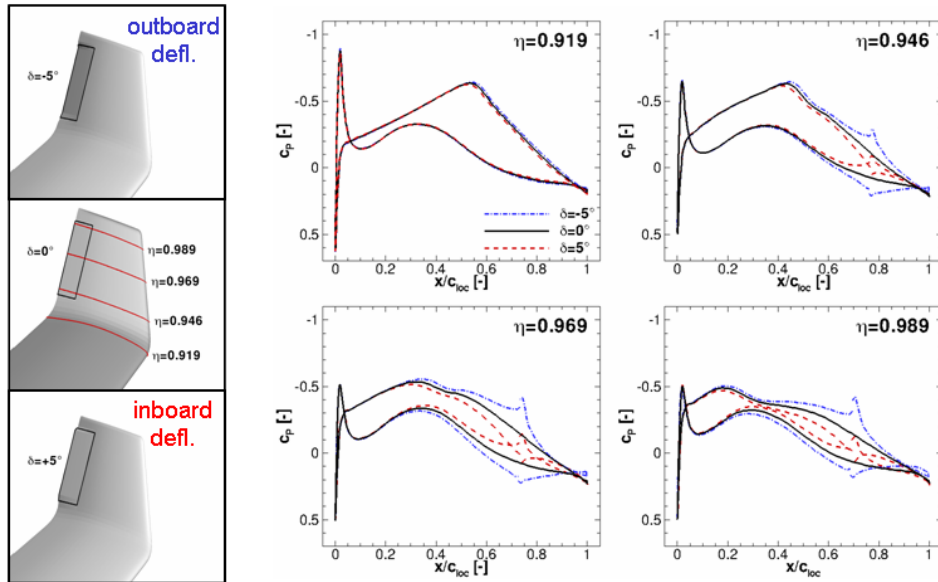

Figure 11: Winglet pressure distribution of spanwise slices for different CS deflections of the modified wing-winglet configuration (Ma=0.83, q/E=$0.60 \cdot 10^{-6}$, Re=$23.5 \cdot 10^6$, α=0°)

Corresponding to the pressure drop at a positive inclined ACS the lift reduces in the winglet vicinity, as shown on the left of Figure 12. On the right of Figure 12 the resulting

deformational magnitudes are illustrated, revealing a maximal influence range of $2.1mm$ in vertical displacement and 0.15^o in aerodynamic twist, due to the static ACS.
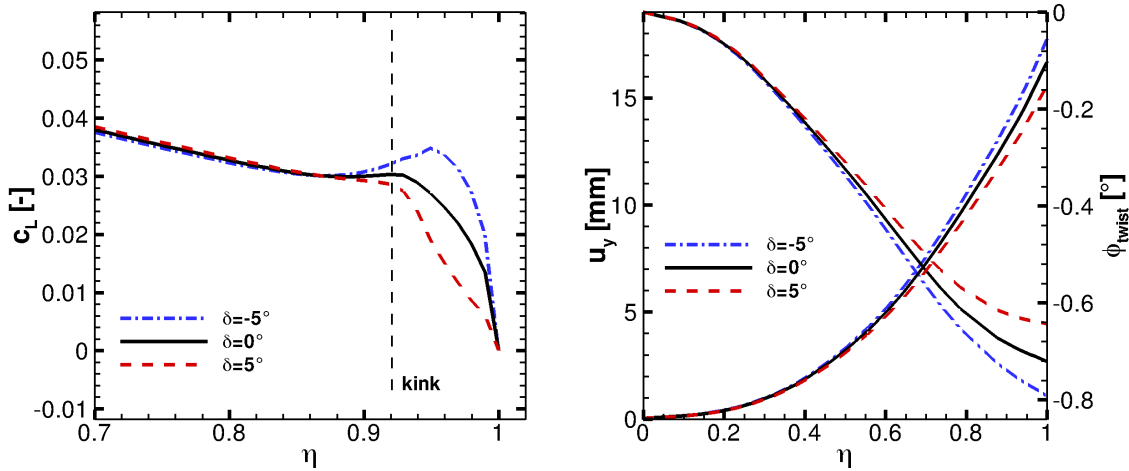

Figure 12: Influence of static ACS on spanwise lift distribution and deformation, left: spanwise lift distribution in winglet vicinity, right: spanwise vertical displacement and aerodynamic twist (Ma=0.83, q/E=$0.60 \cdot 10^{-6}$, Re=$23.5 \cdot 10^6$, α=0°)

The gaps between the control surface and the winglet are disregarded in the computations.

5 PREDICTION OF DYNAMIC AEROELASTIC MODEL BEHAVIOUR

Dynamic aeroelastic problems are characterised by the interaction of the wing structure with the ambient flow. Oscillation frequencies and damping of the structure change due to the interaction with the flow. It is therefore essential to verify that the wing model holds positive aerodynamic damping for the planned flow conditions.

In order to study the vibrational decay behaviour of the wing-winglet model about the aeroelastic equilibrium configuration, static aeroelastic computations with additional loads subjected to the model structure have to be conducted beforehand, as shown in Figure 13. The respective forces and moments were defined such that the initiated shape deviation corresponds to combinations of 1st, 2nd flap-bending and 1st torsion dominated mode shape.
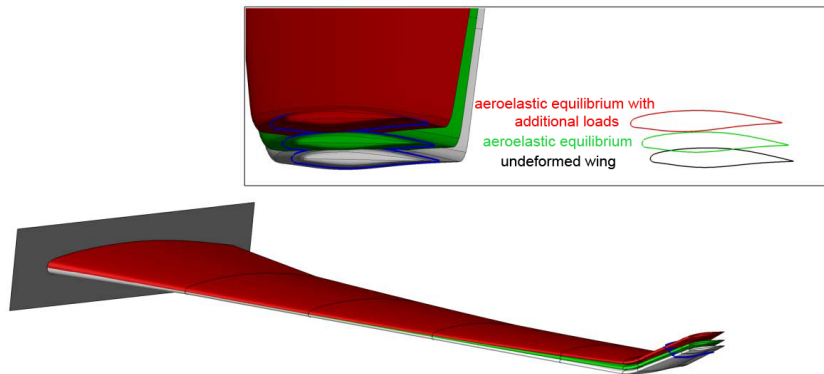

Figure 13: Different initial AECs of the wing with and without subjecting the wing with additional loads

After the aeroelastic equilibrium is obtained, the additional loads are suddenly removed

initiating the unsteady simulation. The resulting imbalance between inner structural re-action forces and outer aerodynamic forces lead to vibrational motions. Figure 14 shows exemplarily time histories of vertical displacement u_{tip} and pure structural torsion $\phi_{T,tip}$ at wing tip, the latter denoting the rotation of cross-sections oriented perpendicular to the elastic axis. The initial amplitude of bending deformation is about $20mm$, the torsional vibration starts with an amplitude of 0.4^o. Both vibrational motions reveal positive aero-dynamic damping at imposed flow conditions, whereas the torsional tip motion oscillates with higher frequency than the translational one.
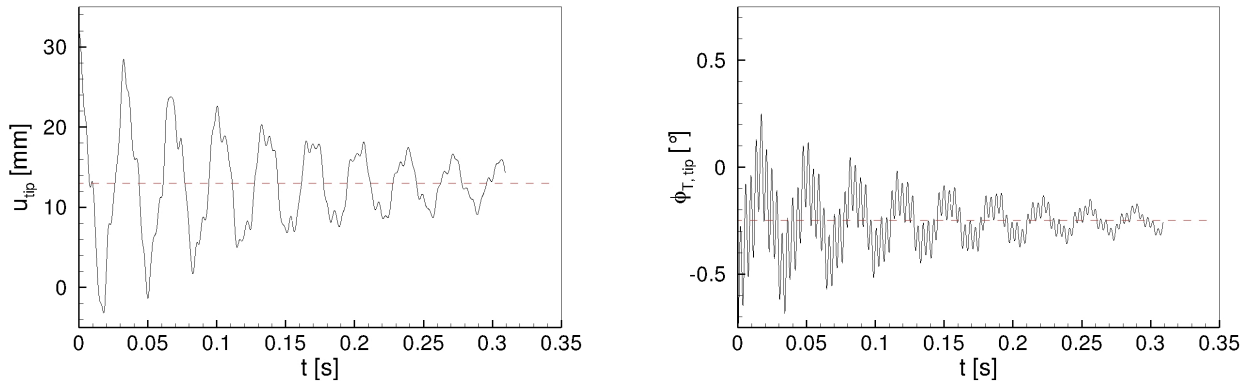

Figure 14: Time histories of displacement u_{tip} and $\phi_{T,tip}$ on the left and right, respectively, during vibration decay

The vibrational decay test was conducted for all flow conditions mentioned before and compared to numerical results of the HIRENASD wing. Some of the simulation results regarding the influence of the Mach number on frequencies and related aerodynamic damping for 1st, 2nd and 5th eigenmode are depicted in the left and right column of Figure 15. The comparison shows a distinct higher frequency of the wing-winglet model compared to the HIRENASD model for the 1st and 2nd eigenmode and a lower one for the 5th eigenmode. The damping factors on the contrary exhibit higher values of the wing-winglet model for all shown eigenmodes. Considered only the frequency of the 1st eigenmode, both distributions increase slightly and decrease after Ma=0.85. The corresponding damping factors decrease at first and increase after Ma=0.83, whereas the ASDMAD model shows a higher gradient. In the middle row of Figure 15 the frequencies and damping factors of the 2nd eigenmode increase monotonously. However, the values vary only little indicating a weak dependence on Mach number changes in the investigated range. The frequencies and damping factors of the 1st torsion dominated eigenmode show an opposed behaviour, while one magnitude increases monotonously the other decreases. Nevertheless, the dependence on Mach number variations remains small. This investigation was also conducted with different magnitudes of loads factor which will be discussed in the following.

In Figure 16 differences of 1st, 2nd and 5th eigenmode between simulation results of the ASDMAD and HIRENASD wing are depicted over the Mach number. Furthermore, the influence of the loads factor variation (q/E=$0.22 \cdot 10^{-6}$, $0.34 \cdot 10^{-6}$, $0.48 \cdot 10^{-6}$ and $0.60 \cdot 10^{-6}$) is identified herein. The distribution of the frequency differences for the 1st eigenmode are illustrated in the top left diagram of Figure 16. It appears that the
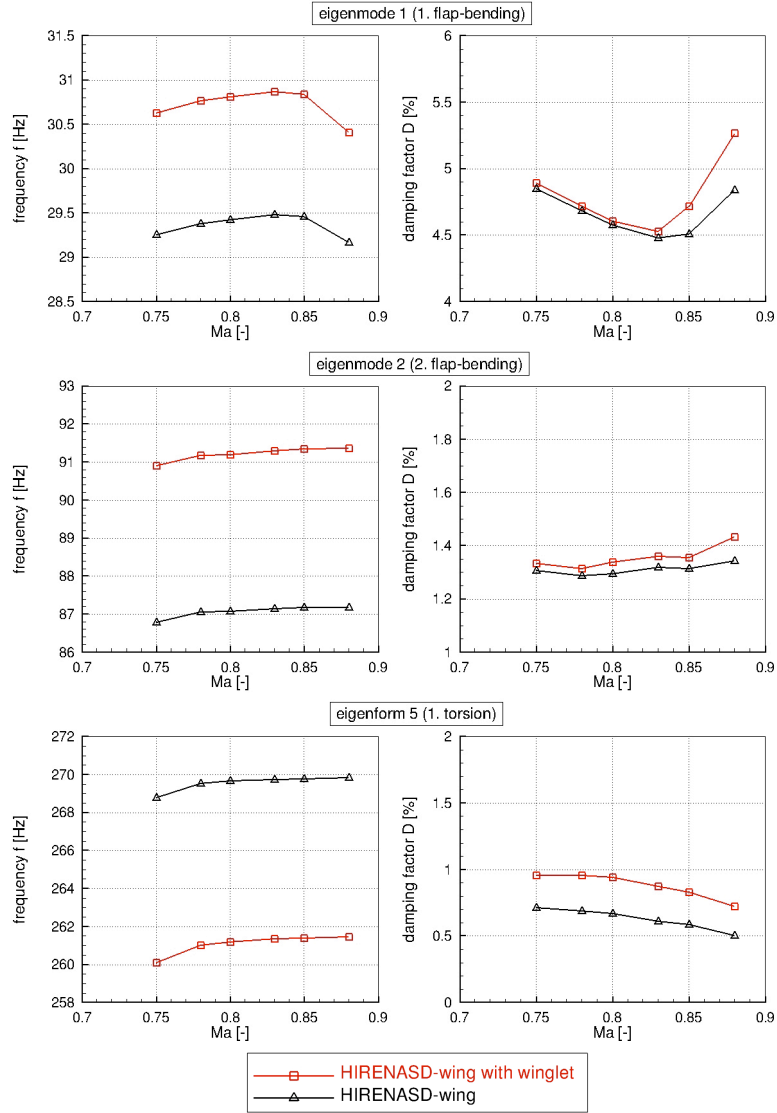
11

Figure 15: Influence of Mach number Ma on frequencies and aerodynamic damping factors of 1st, 2nd and 5th eigenmode of the wing-winglet model in comparison with the original HIRENASD model (Re=23.5 $\cdot$ 10^6, q/E=0.48 $\cdot$ 10^{-6} and α=0.0°)

eigenfrequencies of the wing-winglet configuration increases stronger than the ones of the HIRENASD wing with growing loads factor in the Mach number range Ma=0.75 to 0.85 with an exception for q/E=0.60 $\cdot$ 10^{-6}. At this value, the difference already drops after Ma=0.80 slightly, which becomes more pronounced above Ma=0.85 for all curves. The top right of Figure 16 exhibits the difference in damping factors for the 1st eigenmode, which verifies the stronger damping factor increase of the ASDMAD wing in comparison with the original HIRENASD wing discussed in Figure 15. The middle row of Figure 16 is related to the 2nd flap-bending dominated eigenmode. The differences on the left indicate the independence to Mach number and loads factor variation, whereas the distribution of the damping factor on the right shows weak dependency with increasing values, which is also in accordance to the results examined previously. The bottom row of Figure 16 highlights the results for the 5th eigenmode. Whereas the differences of the frequencies remain almost constant for the highest investigated loads factor within the regarded Mach
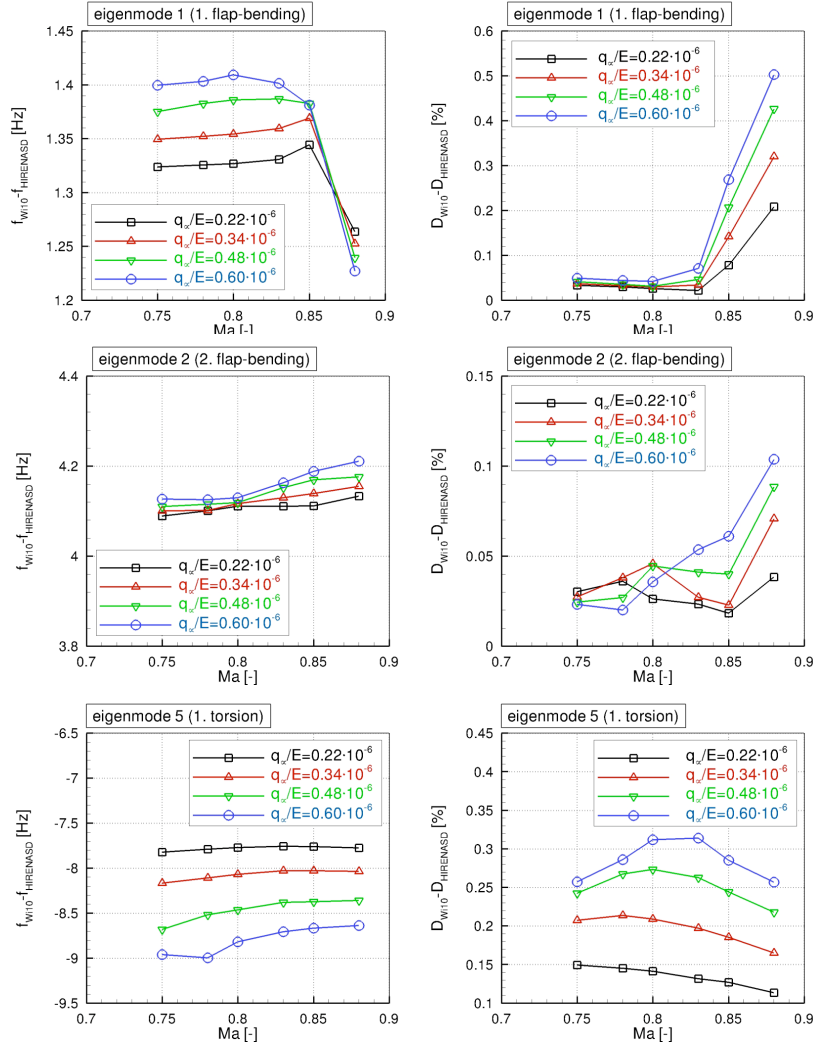
12

Figure 16: Influence of Mach number Ma on frequencies and aerodynamic damping factors of 1st, 2nd and 5th eigenmode ($Re=23.5 \cdot 10^6$, $q/E=0.48 \cdot 10^{-6}$ and $\alpha=0.0°$)

number range, the dependence gets more important with decreasing q/E. The differences of the damping factors on the other hand change less with change of Mach number for the two lower loads factors and more for the two highest loads factors investigated.

The results presented here were conducted at a constant angle of attack $\alpha=0.0^o$. But the dependence of characteristic vibrational parameters on angle of attack was studied by additional simulations for $\alpha=2.0^o$ and 4.0^o as well. These revealed only a small impact on frequency and aerodynamic damping of the 1st bending dominated eigenmode whereas higher modes remained almost unaffected by varying angles of incidence.

5.1 Influence of the Static Control Surface on Dynamic Aeroelastic Response Behaviour

In Figure 17 exemplary results of a directly simulated dynamic aeroelastic response after initial static deflection by an additional force which is suddenly removed are shown. The tip deflection, torsional twist at wing tip, flow induced vibration frequency shifts and aerordynamic damping parameters of the 1st and 2nd flap-bending and 1st torsion domi-

nated modes were determined and confronted to the respective values of the configuration without winglet (black curve). For the model with WACS the CS deflections were chosen $\delta=0^o$ (red curve) and $\delta=5^o$ (blue curve). The changes in frequency shifts with respect to vacuum properties are clearly noticeable for all three modes due to the additional winglet, whereas only the damping rate of the 5th mode changes significantly. The influence of the CS inclination appears only small.

Frequency shifts w.r.t. to vacuum properties Δf [Hz]	Wing only		Wing-Winglet δ=0°		Wing-Winglet δ=5°
1st flap-bend. dom.	2.597	+5%	2.733	<1%	2.728
2nd flap-bend. dom.	0.318	+23%	0.411	<1%	0.408
1st torsion dom.	-0.434	-57%	-1.011	<2%	-0.996

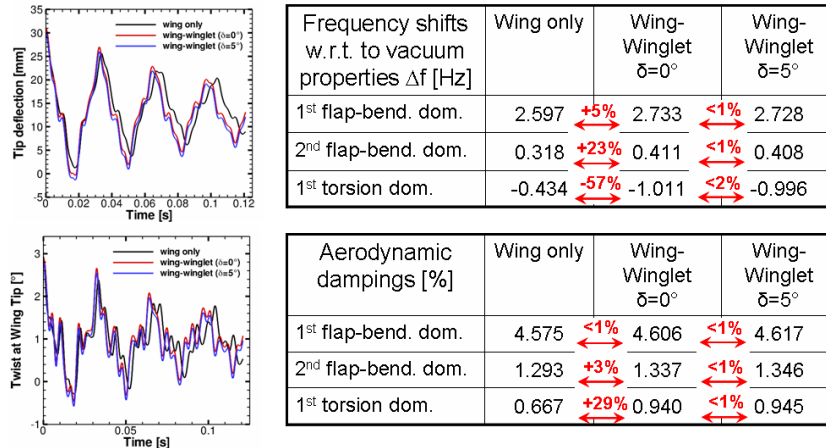| Aerodynamic dampings [%]	Wing only		Wing-Winglet δ=0°		Wing-Winglet δ=5°
1st flap-bend. dom.	4.575	<1%	4.606	<1%	4.617
2nd flap-bend. dom.	1.293	+3%	1.337	<1%	1.346
1st torsion dom.	0.667	+29%	0.940	<1%	0.945

Figure 17: Influence of winglet and ACS deflection on dynamic aeroelastic response behaviour ($Ma=0.80$, $Re=23.5 \cdot 10^6$, $q/E=0.48 \cdot 10^{-6}$ and $\alpha=0.0^o$)

6 SUMMARY

In this paper the numerical prediction of the static and dynamic aeroelastic behaviour of the modified HIRENASD wing was presented. Based on a series of static aeroelastic simulations for different winglet sweeps, the one with about 10° additional sweep relative to the leading edge was selected in a compromise decision between aerodynamic properties and required internal space for the WACS driving mechanism. The differences in lift and deformation magnitudes were revealed due to the additional winglet. The analysis of the static ACS deflection influence proved to be an adequate instrument to manipulate the additional root bending moment due to the winglet. Furthermore, the response behaviour of the modified wing was investigated and frequency shifts and damping rate changes of the 1st, 2nd and 5th eigenmode were determined. Thus, reaveling an increase of frequency shifts with respect to vacuum properties of the 1st and 2nd flap-bending dominated modes and decrease of the 1st torsion dominated mode. The influence of the CS inclination appears only small in this course.

7 REFERENCES

[1] Braun, C.: *Ein modulares Verfahren fuer die numerische aeroelastische Analyse von Luftfahrzeugen.*, Doctoral thesis, Aachen University, 2007,

[2] Ballmann, J., Dafnis, A., Korsch, H., Buxel, C., Reimerdes, H.-G., Brakhage, K.-H., Olivier, H., Baars, A., Boucke, A.: *Experimental Analysis of High Reynolds Number Aero-Structural Dynamics in ETW.* 46th AIAA Aerospace Sciences Meeting and Exhibit, Paper AIAA-2008-841, Reno, Nevada, United States of America, 2008

[3] Reimer, L., Braun, C., Chen, B.-H., Ballmann, J.: *Computational Aeroelastic Analysis and Design of the HIRENASD Wind Tunnel Wing Model and Tests.* In proceed-

ings of the International Forum on Aeroelasticity and Structural Dynamics (IFASD) 2007, Paper IF-077, Stockholm, Sweden, 2007

[4] J. Ballmann et al.: *The HIRENASD project: High Reynolds number aerostructural dynamics experiments in the European Transonic Windtunnel (ETW)*, International Congress of the Aeronautical Sciences 2006, Hamburg, ICAS 2006-5.11.2

[5] Ballmann, J.: *Transonic High Reynolds Number Aero-Structural Dynamics Experiments in the European Transonic Windtunnel (ETW)*, International Forum on Aeroelasticity and Structural Dynamics (IFASD) 2007, Stockholm, 2007, invited keynote lecture

[6] HIRENASD project homepage: https://heinrich.lufmech.rwth-aachen.de/index.php?lang=de\&pg=home

[7] Kroll, N., Faßbender, J. K. (Eds.): *MEGAFLOW – Numerical Flow Simulation for Aircraft Design.* Notes on Numerical Fluid Mechanics and Multidisciplinary Design, Vol. 89, Springer-Verlag, 2005

[8] Kroll, N., Schwamborn, D, Becker, K., Rieger, H., Thiele, F. (Eds.): *MEGADESIGN and MegaOpt – Aerodynamic Simulation and Optimization in Aircraft Design.* Notes on Numerical Fluid Mechanics and Multidisciplinary Design, Springer-Verlag, 2008

[9] Bramkamp, F. D., Lamby, Ph., Müller, S.: *An adaptive multiscale finite volume solver for unsteady and steady flow computations.* Journal of Computational Physics, Vol. 197, pp. 460–490, 2004

[10] Boucke, A.: *Kopplungswerkzeuge für aeroelastische Simulationen.* Ph.D. thesis, RWTH Aachen, 2003

[11] Hesse, M.: *Entwicklung eines automatischen Gitterdeformationsalgorithmus zur Strömungsberechnung um komplexe Konfigurationen auf Hexaeder-Netzen.* Ph.D. thesis, RWTH Aachen, 2006